VU VRIJE UNIVERSITEIT AMSTERDAM

VU Research Portal

Polarity-reversal subduction zone initiation triggered by buoyant plateau obstruction

Almeida, J.; Riel, N.; Rosas, F. M.; Duarte, J. C.; Schellart, W. P.

published in
Earth and Planetary Science Letters
2022

DOI (link to publisher)
10.1016/j.epsl.2021.117195

document version
Publisher's PDF, also known as Version of record

document license
Article 25fa Dutch Copyright Act

Link to publication in VU Research Portal

citation for published version (APA)
Almeida, J., Riel, N., Rosas, F. M., Duarte, J. C., & Schellart, W. P. (2022). Polarity-reversal subduction zone initiation triggered by buoyant plateau obstruction. *Earth and Planetary Science Letters*, *577*, 1-14. [117195]. https://doi.org/10.1016/j.epsl.2021.117195

General rights
Copyright and moral rights for the publications made accessible in the public portal are retained by the authors and/or other copyright owners and it is a condition of accessing publications that users recognise and abide by the legal requirements associated with these rights.

- Users may download and print one copy of any publication from the public portal for the purpose of private study or research.
- You may not further distribute the material or use it for any profit-making activity or commercial gain
- You may freely distribute the URL identifying the publication in the public portal ?

Take down policy
If you believe that this document breaches copyright please contact us providing details, and we will remove access to the work immediately and investigate your claim.

E-mail address:
vuresearchportal.ub@vu.nl

Download date: 22. Sep. 2023

Earth and Planetary Science Letters 577 (2022) 117195

Contents lists available at ScienceDirect

Earth and Planetary Science Letters

www.elsevier.com/locate/epsl

Polarity-reversal subduction zone initiation triggered by buoyant plateau obstruction

J. Almeida [a,b,*], N. Riel [c], F.M. Rosas [a,b], J.C. Duarte [a,b,e], W.P. Schellart [d]

[a] Instituto Dom Luiz (IDL), Faculdade de Ciências, Universidade de Lisboa, Lisboa, Portugal
[b] Departamento de Geologia, Faculdade de Ciências, Universidade de Lisboa, Lisboa, Portugal
[c] Institut fur Geowissenschaften, Johannes Gutenberg-Universitat, Mainz, Germany
[d] Department of Earth Sciences, Vrije Universiteit Amsterdam, Amsterdam, Netherlands
[e] School of Earth, Atmosphere and Environment, Monash University, Melbourne, VIC 3800, Australia

ARTICLE INFO

Article history:
Received 20 December 2020
Received in revised form 28 August 2021
Accepted 31 August 2021
Available online 22 October 2021
Editor: H. Thybo

Keywords:
subduction zones
subduction zone initiation
oceanic plateau
polarity-reversal
numerical modelling
internal force balance

ABSTRACT

Oceanic lithosphere worldwide is younger than ca. 200 Myr, suggesting that it must have been globally recycled by the recurrent formation of new subduction zones since the existence of subduction on Earth. However, postulated subduction zone initiation processes remain difficult to explain in many cases, and the specific geodynamic conditions under which these might occur are still largely unknown. We here use numerical models driven by the internal force balance of a subduction system to better understand the (geo)dynamics governing (intra-oceanic) *polarity-reversal subduction zone initiation*. This initiation mode assumes that the birth of a new subduction zone could be triggered by buoyant plateau-obstruction of a pre-existent one dipping in the opposite direction. Our work provides a new insight on the key geodynamic conditions governing this type of subduction zone initiation and discusses their general compliance with known natural examples.

© 2021 Elsevier B.V. All rights reserved.

1. Introduction

Subduction zone initiation (SZI) is one of the main unsolved problems in modern day plate tectonics theory (Cloetingh et al., 1989, 1982; Crameri et al., 2020; Duarte et al., 2013a; Gurnis et al., 2004; Hall, 2019; Mueller and Phillips, 1991; Stern, 2004; Stern and Gerya, 2018; Zhong and Li, 2019). Most of the oceanic lithosphere worldwide is younger than ca. 200 Myr, which indicates that new subduction zones must be formed sometime after the opening of an ocean (cf. Wilson Cycle concept). SZI is thus mandatory to explain the recurrent recycling of ocean floor lithosphere predicted by global plate tectonics as we know it (Davies, 1992). However, it is (geo)dynamically very difficult to envisage, since its spontaneous (buoyancy-driven) occurrence along old passive margins would require forces of very high magnitude, well above the ones generally acknowledged to exist in nature (Cloetingh et al., 1989; Mueller and Phillips, 1991). Furthermore, no clear examples of Cenozoic SZI along old passive margins are known anywhere on our planet, although some are interpreted to have been formed during Mesozoic times (Crameri et al., 2020; Gurnis et al., 2004). Spontaneous SZI is thus generally seen as unrealistic, since the contribution of tectonic forces is thought as inescapable for any considered tectonic setting on Earth (Arcay et al., 2019; Auzemery et al., 2020; Crameri et al., 2020). To try to solve this fundamental question, several alternative modes of subduction zone initiation have been previously proposed (Crameri et al., 2020; Stern, 2004; Stern and Gerya, 2018). Here, we present a geodynamic numerical modelling study of polarity-reversal subduction zone initiation, which seems to be one of the more common SZI mechanisms in the past 100 Ma (Crameri et al., 2020). Our main goal is to better understand the key combination of forces that, under the simulated modelling constraints, might drive the formation of a new opposite dipping subduction zone, and to evaluate its geodynamic feasibility as a SZI mechanism under similar general conditions in nature.

When a positively buoyant plateau (e.g., an oceanic ridge or a continental fragment) arrives at a subduction trench it resists being dragged downwards along the subduction channel, obstructing it, and ultimately blocking the pre-existent subduction zone. Depending on the thermo-mechanical state of both plates involved, and on the resulting changes in the stress distribution pattern caused by this blocking, a new subduction zone might nucleate either in the back of the obstructing plateau, dipping in the same direction as the original one – *subduction transference* (Stern, 2004; Stern and

* Corresponding author.
E-mail address: jealmeida@fc.ul.pt (J. Almeida).

https://doi.org/10.1016/j.epsl.2021.117195
0012-821X/© 2021 Elsevier B.V. All rights reserved.

Gerya, 2018; Tetreault and Buiter, 2012); or at its front, dipping in the opposite direction – *subduction polarity reversal* (e.g., Hall, 2002; Konstantinovskaia, 2001; Mann and Taira, 2004; Zhang and Leng, 2021). The internal SZI driving forces at play in both these instances have an important horizontal component, rendering the corresponding SZI modes the designation of "horizontally forced" (Crameri et al., 2020).

Based on former (field, analogue and numerical modelling) studies three generic conditions were found indispensable for the formation of a new subduction zone, and acknowledged as common to all previously proposed SZI modes: i) initial bending of the future subducting plate, leading to subsequent underthrusting beneath the future overriding plate (Gurnis et al., 2004; Nikolaeva et al., 2011, 2010); ii) efficient strain localization along a narrow weak zone between the two plates (Gurnis et al., 2004; Lu et al., 2015) facilitated by pre-existing mechanical weaknesses (e.g., transform faults, Uyeda and Ben-Avraham, 1972) and by positive feed-back strain-weakening mechanisms (e.g., chemical weakening or grain-size reduction, Hirauchi et al., 2016) and; iii) propagation of this narrow weak zone across the whole thickness of the lithosphere to form a subduction channel (Gurnis et al., 2004).

While polarity-reversal SZI has been one of the main mechanisms proposed to explain the possible origin of new subduction zones during the Meso-Cenozoic (Buchs et al., 2010; Crameri et al., 2020; Hall, 2002; Konstantinovskaia, 2001; Mann and Taira, 2004; Wright and Wyld, 2011), the fundamental dynamics governing this type of SZI remains poorly understood. Here, we present a series of numerical modelling experiments carried out to gain new insight on the dynamics of this process. We specifically focus on understanding the way through which the internal balance of driving forces in a (pre-existent) subduction zone can be perturbed by the arrival of a buoyant plateau to the trench, as to render polarity-reversal SZI. Our models were conceived to exclusively account for the internal forces at play (i.e., buoyancy vs. viscous resistance) in the absence of any other (externally imposed) ones.

2. Methods

2.1. Numerical code and governing equations

Numerical modelling experiments were carried using the code Underworld (Moresi et al., 2007). Underworld employs a finite element discretization coupled with a particle-in-cell approach to solve the equations of conservation of mass, momentum, and energy (eq. (1)-(3), respectively), assuming conditions of incompressibility:

$$\nabla \cdot \mathbf{v} = 0 \tag{1}$$

$$\nabla \cdot \boldsymbol{\sigma} = \rho \mathbf{g} \tag{2}$$

$$\rho C_p \left(\frac{\partial T}{\partial t} + \mathbf{v} \cdot \nabla T \right) = \kappa \nabla^2 T + H_s + H_A \tag{3}$$

in which $\mathbf{v}$ is the velocity vector, $\boldsymbol{\sigma}$ the stress tensor, ρ the density, $\boldsymbol{g}$ the gravity acceleration vector, κ the diffusivity, T is the temperature and C_p the specific heat. The shear heating (H_S) and the adiabatic heating (H_A) in Equation (3) above are respectively defined as:

$$H_s = \sum \left[\boldsymbol{\sigma}' \cdot \dot{\boldsymbol{\varepsilon}} \right]_{ij} \tag{4}$$

$$H_A = \frac{-T\alpha \mathbf{v_y} g}{c_p} \tag{5}$$

in which, $\boldsymbol{\sigma}'$ represents the deviatoric stress tensor, $\dot{\boldsymbol{\varepsilon}}$ is the strain rate tensor, α the coefficient of thermal expansion and $\mathbf{v_y}$ the vertical velocity. The stress tensor is defined by:

$$\boldsymbol{\sigma} = \boldsymbol{\sigma}' - P\mathbf{I} \tag{6}$$

with P as the pressure and $\mathbf{I}$ the identity tensor. The deviatoric stress tensor ($\boldsymbol{\sigma}'$) is defined as a function of both strain rate ($\dot{\boldsymbol{\varepsilon}}$) and effective viscosity (η_{eff}):

$$\boldsymbol{\sigma}' = 2\eta_{eff}\dot{\boldsymbol{\varepsilon}} \tag{7}$$

The strain rate tensor ($\dot{\boldsymbol{\varepsilon}}$) is in turn defined as:

$$\dot{\boldsymbol{\varepsilon}} = \frac{1}{2}[\nabla \mathbf{v} + (\nabla \mathbf{v})^T] \tag{8}$$

and the effective viscosity is calculated by:

$$\eta_{eff} = A^{-\frac{1}{n}} \dot{\varepsilon}_{II}^{\frac{1}{n}-n} \exp\left(\frac{E_a + V_a P}{nRT}\right) \tag{9}$$

with A as the pre-exponential factor, $\dot{\varepsilon}_{II}$ the second invariant of the strain rate tensor, n the stress exponent, E_a the activation energy, V_a the activation volume and R the universal gas constant.

Plastic flow is implemented in all models assuming a Drucker-Prager yield criterion (Drucker and Prager, 1952), according to which a given material is set to yield plastically when stress surpasses a prescribed limit (yield value):

$$\sqrt{\boldsymbol{\sigma}'_{II}} = p \sin(\phi) + C\cos(\phi) \tag{10}$$

in which $\boldsymbol{\sigma}'_{II}$ is the second invariant of the deviatoric stress tensor, ϕ the internal friction angle and C the cohesion. When materials reach the yield stress, they are linearly softened until ϕ and cohesion reach 10% of the original value.

Plate age dependence of the thermal profiles follows the plate cooling model:

$$T = T_0 + (T_1 - T_0)\left[\frac{y}{y_{Lo}} + \frac{2}{\pi} \sum_{n=1}^{\infty} \frac{1}{n} \exp\left(\frac{\kappa n^2 \pi^2 t}{y_{Lo}^2} \right) \sin\left(\frac{n\pi y}{y_{Lo}} \right) \right] \tag{11}$$

in which T_0 is the temperature at the surface of the model (set to 273 K), T_1 is the temperature at the lithosphere-asthenosphere boundary (y_{Lo}) set to 1473 K, y is the depth, and t is the age of the plate. All material densities are also temperature dependent according to:

$$\rho = \rho_0[1 - \alpha (T - T_0)] \tag{12}$$

in which ρ_0 is the density of the material at the reference temperature T_0.

2.2. Initial model setup and modelling approach

A set of 2D numerical modelling experiments was conceived (Fig. 1A), in which all model kinematics (i.e., the movement of the plates and the resulting flow in the sub-lithospheric mantle) are the result of the internal balance between the slab negative buoyancy driving force and the counteracting viscous resistance (e.g., Schellart, 2017; Stegman et al., 2010). No external forces (e.g., resulting from prescribed boundary conditions) were implemented in any of the models, which are thus fundamentally controlled by the way this internal force balance changes with time.

The considered (overriding vs. downgoing) plate age contrast was systematically varied, with initial overriding plate (OP) ages ranging between 10 and 70 Myr, for 10 Myr intervals. The assumed initial age variation for the downgoing plate (DP) was between 10 and 110 Myr, also for 10 Myr intervals (Fig. 2). A total of 77 numerical simulations was thus investigated, comprising all resulting

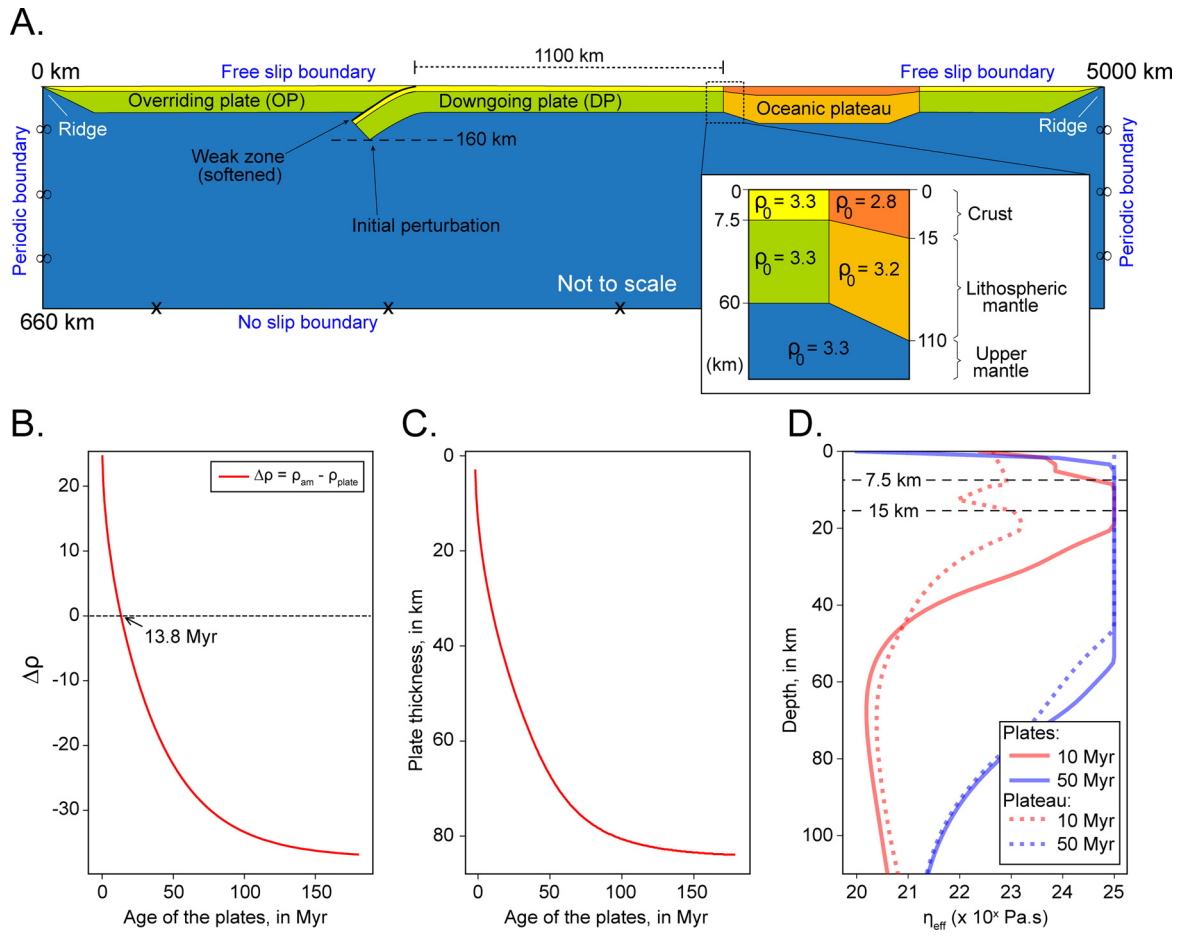

Fig. 1. A. Model setup for the experimental initial state (not to scale): schematic representation of the geometric configuration, model dimensions and prescribed boundary conditions (BCs). Inset shows comparative (normal plate vs. plateau) *reference* densities (ρ_0 in g/cm^3) initially assumed for the crust, lithospheric mantle and asthenosphere. Note that unit shapes and corresponding ρ_0 values in A do not reflect plate ageing, nor associated cooling and implied *effective* lithospheric densities and thicknesses, which ultimately determine the changing buoyancy of the lithospheric plates relatively to its underlying mantle. **B. Effective buoyancy**, **C. Effective maximum lithospheric thickness** as a function of plate age. Effective buoyancy is expressed by the density contrast between the asthenosphere and the lithospheric mantle: $\Delta_\rho = \rho_{am} - \rho_{plate}$. Effective lithospheric thickness is given by the depth of the 1473 K (1200° C) isotherm. The depicted time-dependent evolution of both parameters is determined by the assumed plate cooling model (Equations (11) and (12)), and **D. Strength-depth profiles** for plates (solid lines) and corresponding plateaus (dashed lines) with differently assumed initial ages of 50 (in blue) and 10 Myrs (in red). Strength of the plates is given by effective viscosity (η_{eff}). (For interpretation of the colours in the figure(s), the reader is referred to the web version of this article.)

combinations of initial OP vs. DP ages. This variety expresses different initial rheological and density contrasts between the two plates in each case, hence bearing a decisive influence on the final geodynamic outcome that follows from plateau accretion and collision (see Fig. 2).

The considered 2D model domain is of 5000 × 660 km, with its maximum depth corresponding to the upper-lower mantle transition (see Fig. 1A) and was discretized using a uniform 1536 × 384 grid. A 110 km thick positively buoyant plateau was set fixed to the subducting slab in the initial stage of all the experiments at 1100 km from the subduction trench (see inset of Fig. 1A). In the plateau, both the crust and lithospheric mantle were initially set as positively buoyant (with ρ_0 reference densities of 2800 and 3200 kg/m^3, respectively) relative to the denser OP and DP, and to the asthenosphere (all with $\rho_0 = 3300$ kg/m^3 - see Table 1). A thin (ca. 15 km) weak zone was set between the overriding and downgoing plates, accounting for a pre-existent subduction channel. Subduction was triggered in all models by the negative buoyancy of the DP implied by the initial model configuration, in which the foundering of the tip of the subducting slab was set at a maximum depth of 160 km (see Fig. 1A).

The initial temperatures for both plates were defined in accordance with the plate cooling model (eq. (11)), in which T is

Table 1
Parameters used in the definition of the non-linear (thermal dependent) model rheology/density configuration. The density (ρ_0) parameters represent the density at reference temperature (T_0, see Equation (11)).

Parameters	Values	Reference
Expansibility, α (K^{-1})	3.00×10^{-5}	-
Diffusivity, κ (m^2 s^{-1})	1.00×10^{-6}	-
Heat capacity, C_p (J kg^{-1} K^{-1})	1.00×10^{3}	-
c_{crust} (MPa)	20	(Hui et al., 2014)
c_{mantle} (MPa)	30	(Hui et al., 2014)
Φ_0 (degrees)	~ 14	(Gerya et al., 2008)
$T_{surface}$ (K)	273	-
T_{base} (K)	1473	-
$\rho_{0\ oceanic\ crust}$ (kg m^{-3})	3300	-
$\rho_{0\ lithospheric\ mantle}$ (kg m^{-3})	3300	-
$\rho_{0\ asthenosphere}$ (kg m^{-3})	3300	-
$\rho_{0\ plateau\ crust}$ (kg m^{-3})	2800	-
$\rho_{0\ plateau\ mantle}$ (kg m^{-3})	3220	-
$A_{plateau\ crust}$ (MPa^{-n} s^{-1})	1.00×10^{-7}	(Ranalli, 1997)
$A_{upper\ mantle}$ (MPa^{-n} s^{-1})	5.49×10^{4}	(Ranalli, 1997)
$n_{plateau\ crust}$	2.00	(Ranalli, 1997)
$n_{plateau\ mantle}$	3.50	(Ranalli, 1997)
$E_{a\ plateau\ crust}$ (J mol^{-1})	1.50×10^{5}	(Ranalli, 1997)
$E_{a\ upper\ mantle}$ (J mol^{-1})	5.30×10^{5}	(Ranalli, 1997)
V_a (m^3 mol^{-1})	1.00×10^{-6}	(Ranalli, 1997)

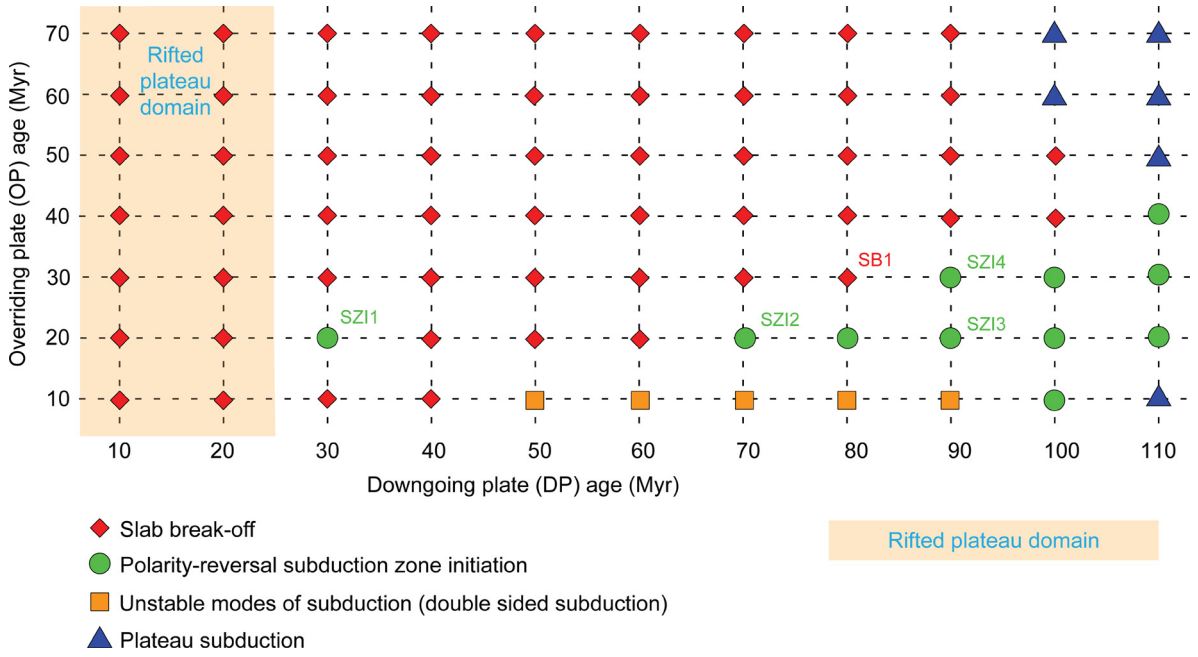

Fig. 2. Graphic grid depiction of all 77 plate age combinations considered in the carried out numerical modelling experiments. Vertical and horizontal axes represent the initial ages prescribed to the overriding and downgoing plates, (OP and DP) respectively. The symbols at the nodes of the grid represent the (general) results: **red diamonds** correspond to numerical model results that did not yield subduction polarity-reversal, and in which the initial subduction was always terminated by DP slab break-off after the arrival of the plateau at the subduction trench; **Green circles** correspond to numerical modelling results that yielded polarity-reversal subduction zone initiation; **Oranges squares** represent (transient, unstable) double-sided subduction, which was not investigated in detail in the present study; **Dark blue triangles** represent plateau subduction events (also not investigated in detail in the present study). The **shaded light-orange domain** corresponds to the results in which rifting was observed to occur in one of the plates (generally the DP).

obtained as a function of both depth and time (plate age). Using this thermal model and the assumed density dependency on temperature (eq. (12)), the effective plate density contrast between the plate and the underlying asthenosphere can be calculated (eq. (13)):

$$\Delta\rho^{\text{plate}}_{\text{asthenosphere}} = \rho_{\text{am}} - \rho_{\text{plate}} \tag{13}$$

with ρ_{am} as the density of the sub-lithospheric mantle and ρ_{plate} the average density of the plate. The resulting description of plate density contrast as a function of time (Fig. 1B) shows that any plate becomes denser than the underlying mantle (i.e., negatively buoyant) after only ca. 14 Myr. The effective (rheological) thickness of the lithosphere (set by the 1473 K isotherm), and the way it depends on time, are also deduced from the same plate cooling model (eq. (11)) showing a consistent non-linear increase of plate thickness with its age (Fig. 1C).

The trailing edges of both plates are tapered, with the basal lithosphere isotherm bulging upwards near the left and right model boundaries, defining a pair or mantle upwelling ridge centres (see Fig. 1A). This allows for free lateral migration of both plates, ensuring that slab negative buoyancy force and mantle viscous resistance act as the only main forces in our models (besides only minor ridge push at the lateral boundaries). It also prevents the otherwise strong downwelling of cooled material formed at the edges of the model, which would artificially perturb the mantle flow.

The model rheology of the oceanic plateau crust follows a plagioclase creep law (Ranalli, 1997), while the remaining model materials follow the dry peridotite law (Ranalli, 1997). Consequently, for younger plateaus (i.e., with higher thermal gradients), the crust of the plateau is weaker than the surrounding oceanic plate crust (see Fig. 1D, dotted vs solid red lines). For older plates (i.e., with lower thermal gradients), the strength profile of the plateau and oceanic plates is almost identical (see Fig. 1D, solid vs dotted blue lines).

The initial subduction interface (softened weak zone in Fig. 1A) is defined by an isoviscous rheology (with a constant low viscosity of 10^{20} Pa·s) to achieve early on high strain localization in the subduction channel. This soft material channel is subducted in the early stages of the experiments and bears no relevant role in any of the model results.

All assumed parameters for the different considered model materials are presented in Table 1.

2.3. Boundary conditions (BC)

The models have periodic boundary conditions along the horizontal axis (eq. (14), Fig. 1A). Accordingly, material escaping through one of the lateral (vertical) boundaries is prescribed to re-enter the model across the other (opposite) one with the same velocity value:

$$\vec{v}_{x-a} = \vec{v}_{x+a} \tag{14}$$

where a is the width of the model. This allows for subduction slab roll-back/-forward and implied trench migration, as closed lateral boundaries hinder such motions in 2D models since no toroidal (return) mantle flow from beneath the slab is possible in these cases (Schellart, 2004). Horizontal free-slip BC were ascribed to the model top boundary (eq. (15)) deterring vertical escape/motion of material across this boundary (see discussion in Appendix A, paragraph g). No-slip BC, defined by Equation (16), were instead implemented along the model bottom wall. Such basal BC account for the sharp viscosity contrast along the 660 km upper-lower mantle transition. This approximates slab anchoring at this discontinuity without accounting, however, for further subduction across this interface.

$$\vec{v}_y = \vec{0} \tag{15}$$

$$\vec{v}_x = \vec{v}_y = \vec{0} \tag{16}$$

Thermally, the model top wall was prescribed to correspond to the 273 K (0° C) isotherm, while the bottom boundary was set to correspond to 1873 K (1600° C).

3. Results

The initial subduction of the DP always drives the (thicker, buoyant) oceanic plateau to the trench, where it resists being further dragged downwards, obstructing the subduction channel, and ultimately bringing this initial subduction to an end (red diamonds in Fig. 2). In most cases, this obstruction leads to slab break-off (Fig. 3A-B, see Supplementary Video 1). This involves total tearing of the subducted DP from the adjacent buoyant plateau, with relatively little bending of the OP (Fig. 3B).

In a smaller number of cases (green circles in Fig. 2), the original OP is significantly bent and underthrust beneath the original DP, ultimately leading to the birth of a new subduction zone dipping in the opposite direction (Fig. 3C, see Supplementary Video 5). This polarity-reversal SZI was observed only in 11 numerical experiments ($\sim$ 14% of the cases) for a variety of different initial age combinations between the OP and the DP (green circles in Fig. 2 and Supplementary Videos 3-6). These initial ages influence the buoyancy, thickness, and strength of both plates at the time of the arrival of the plateau at the subduction trench (or plateau docking, Fig. 4). Under our modelling setup, the dynamic conditions that eventually yield polarity-reversal SZI result mostly from the combination of younger overriding plates and older (stronger) downgoing plates. The results also show (Fig. 4 and Supplementary Videos) that polarity-reversal SZI requires the DP to be negatively buoyant relatively to both the asthenosphere and the OP (see location of green circles in Fig. 4 within the DP negative buoyancy domain). Accordingly, polarity-reversal SZI was never observed for OP with an age at docking greater than ca. 64 Myr or with an effective strength higher than ca. 10^{23} Pa·s (Fig. 4A and 4B, respectively).

Unstable double-sided subduction was observed in $\sim$ 6% of the results in models with initial OP ages = 10 Myr (orange squares in Fig. 2, Supplementary Video 2). It always occurred at very early stages in our simulations, as a transient unstable result, when the buoyant plateau was still several hundreds of kilometres away from the trench. It may represent a transient mode between different, oppositely facing single-sided subduction zones as shown in previous whole-mantle geodynamic studies (Crameri et al., 2014; Crameri and Tackley, 2015), or it could simply correspond to a model artefact arising from the adopted free-slip top boundary conditions (see Appendix A, paragraph g). In any case, this double-sided mode of subduction has never been recorded in the Earth's lithosphere (Gerya et al., 2008) and its specific study it is out of the scope of the present paper.

4. Discussion

4.1. General conditions favouring polarity-reversal SZI

The obtained model results show that triggering of polarity-reversal SZI at the time of plateau docking is favoured by older (thicker and more negatively buoyant) DPs relatively to the corresponding OPs (green circles in Fig. 4A). The resulting rheological plate configuration must also comply with the following main (geodynamic) conditions (Figs. 3–5):

1) The crust of the OP must be weak enough to be bent upwards and locally underthrusted (beneath the DP), with intense strain localization along the resulting main antithetic shear zone enabling the formation of a new proto-subduction channel (Fig. 3-C1, 4B, and 5A). This is generally attained even when slab break-off rather than polarity-reversal SZI occurs (see Fig. 3B and Supplementary Videos). In most cases the DP detaches from the buoyant plateau, and the resulting gap is either to be closed again, as the OP collides against the plateau during the prevailing slab break-off outcome (Fig. 3-B1), or to remain open resulting in the new opposite dipping subduction channel in the less common situation of polarity-reversal SZI (Fig. 3-C1).
2) The OP must also be thin and weak enough to be able to bend downwards, promoting the collapse of the original subduction channel, its closure, and the definite coupling with the DP (Fig. 3-C2, 4B and 5B). Results indicate that OPs with a docking age greater than $\sim$ 64 Myr render plates too strong and thick to be able to accommodate the required plate bending, regardless of how negatively buoyant they might be (see Fig. 4). In fact, plateau subduction (blue triangles in Fig. 2 and 4, see also Supplementary Video 7) occurs in models with older (stronger) OPs, which suggests that under these conditions even the sinking of the positively buoyant plateau is more prone to occur than the bending and underthrusting of the (thick and strong) overriding plate.
3) The coupled (welded) OP and DP must yield a slab-pull strong enough to bend down the OP with a small enough bending radius so that the newly formed subduction channel is not closed, ultimately leading to the development of a new subduction zone with an opposite polarity (see Fig. 3-C3 and Supplementary Videos). The welding between the two plates, controlled by the rheology of the DP crust (the interface between the plates), thus seems to be the critical factor for the occurrence of polarity-reversal SZI.

More detailed manifestations of these main geodynamic constraints are illustrated by the interpretation of the obtained polarity-reversal outcomes as follows.

4.2. Initial subduction channel collapse and plate welding

Polarity-reversal subduction zone initiation was observed in experiments with different initial DP ages, but only for cases in which the DP was consistently older than the OP (see Fig. 2). In these situations, different original subduction dip angles and bending radii were observed, depending on the strength and thickness of the DP implied by its assumed initial age (Irvine and Schellart, 2012). Accordingly, younger (weaker and thinner) DPs yielded steeper subductions zones with a tighter bending radius (Fig. 6A), while older (stronger and thicker) DPs are more difficult to bend, forming gentler dipping subduction zones with a wider bending radius (Fig. 6B). For all polarity-reversal outcomes, compression between the two plates (and implied increase in friction along the subduction channel) led to initial folding of the OP against the stronger DP (Fig. 6-A1 and B1). The amplification of this folding at the time of plateau docking produced a downwards clockwise rotation of the tip of the OP, causing the initial subduction channel to collapse (Fig. 6-A2 and B2 and respective insets). Simultaneously, the OP progressively cut through the weaker plateau, eventually rupturing the DP to nucleate a new subduction channel. With the definite shutdown of the initial subduction zone the OP and the DP became welded. This increased the (buoyancy-driven) sink of both plates in the ambient mantle (higher slab-pull), facilitating the tight bending of the OP and the continued propagation of the newly formed subduction channel (Fig. 6-A2, B2 and B3). Polarity-reversal SZI was only observed for the cases in which this OP-DP welding was observed, showing its crucial importance for the triggering of this mode of subduction zone initiation.

Our results show that the initial folding of an OP against a stronger DP, the associated occurrence of antithetic thrust-shearing

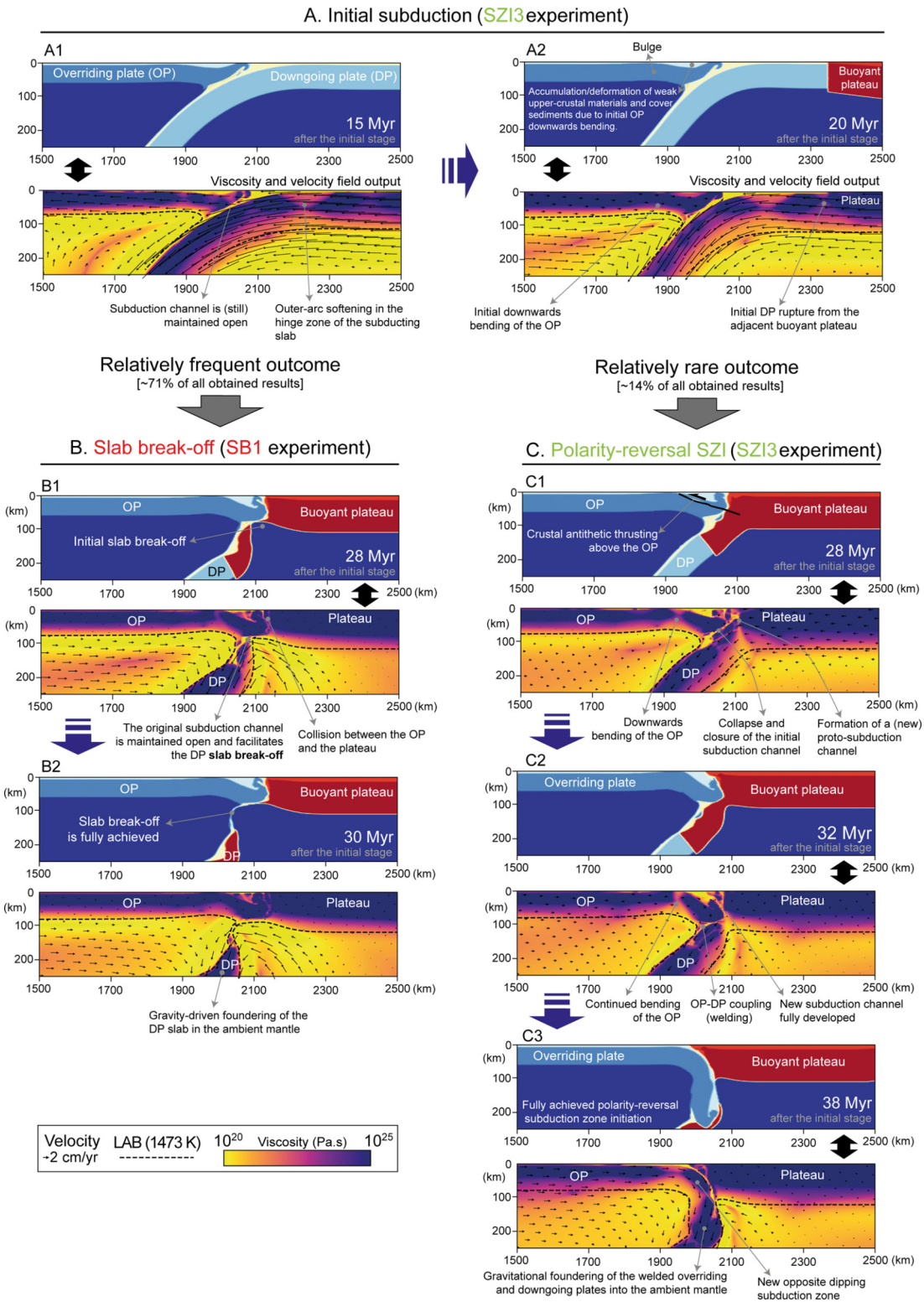

Fig. 3. Numerical model results: comparison between model evolution leading to slab break-off vs. polarity-reversal subduction zone initiation (geometry, viscosity, and velocity outputs are shown for each stage). **A. Initial steady-state subduction** between the arrival of the DP at the 660 km interface and the arrival of the buoyant plateau at the trench. A1-A2: The OP is slightly bent downwards, and DP starts to break apart from the adjacent buoyant plateau. Due to the initial OP downwards bending weak upper-crustal materials and cover sediments are accumulated and deformed (shortened and thickened) in a tectonically subsiding basin located in the arc-forearc region. **B. Slab break-off** outcome (observed in ~ 71% of the experimental results). B1-B2: OP is not bent any further and collides with the plateau closing a potential new subduction channel; the original subduction channel is maintained open and propagates the rupture of the DP; slab break-off is complete with total separation of the DP that sinks into the ambient mantle. **C. Polarity-reversal SZI** outcome (observed in ~ 14% of the experimental results). C1: Continued downwards bending of the OP and crustal antithetic thrusting above this plate; initial collapse of the original subduction channel and simultaneous opening of a new proto-subduction channel. C2: Further bending of the OP; full closure of the old subduction channel and OP-DP welding; continued development of the new subduction channel dipping in the opposite direction. C3: Completion of polarity-reversal SZI; subduction of the (original) OP is driven by negative-buoyancy foundering of both the OP and the DP in the ambient mantle. **OP** - Overriding pate; **DP** - Downgoing plate; **Thin black arrows** - velocity field; **Contour dashed black lines** - lithosphere/asthenosphere thermal boundary (LAB, marked by the 1473 K isotherm). Experiments SB1 and SZI3 are also fully depicted in Supplementary Videos 1 and 5, respectively.

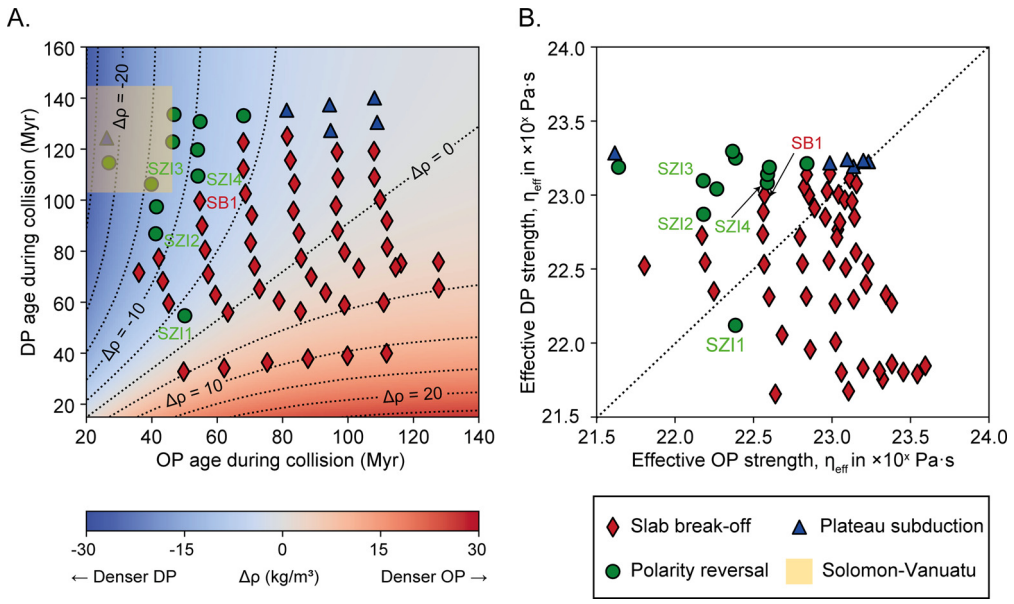

Fig. 4. A: Depiction of the general numerical modelling outcomes (polarity-reversal, slab break-off and plateau subduction) as a function of OP and DP ages at the time of the arrival of the plateau at the trench (plateau docking). The coloured background and associated dashed lines represent the buoyancy contrast field between the OP and the DP, which values are defined as $\Delta\rho_{DP}^{asthenosphere} - \Delta\rho_{OP}^{asthenosphere}$ (units in kg/m^3). Note that $\Delta\rho_{OP}^{asthenosphere} = \rho_{asthenosphere} - \rho_{OP}$ and $\Delta\rho_{DP}^{asthenosphere} = \rho_{asthenosphere} - \rho_{DP}$ are both negative, given that both the OP and the DP are negatively buoyant relatively to the asthenosphere since ~ 14 Myr of age (see Fig. 1B). The bluish negative part of the field thus represents conditions in which the DP is more negatively buoyant than the OP. Note also that most of the polarity-reversal SZI results fall into this negative subdomain. The yellow rectangle shows the plate age range for the occurrence of polarity-reversal SZI in the Solomon-Vanuatu natural example. **B:** Depiction of the same general numerical modelling outcomes as a function of OP and DP effective strength (η_{eff}) at the time of plateau docking.

above the OP (nucleation of a proto-subduction channel) and the rupture of the DP from the adjacent plateau, are all quite common for different OP-DP age combinations (even during the frequent outcome of slab break-off). But it is only when OP-DP welding occurs that the shallower shear zone representing the proto-subduction channel can propagate downwards, rupturing across the whole lithosphere and maturing into a new opposite dipping subduction zone. Thus, our numerical results suggest that polarity-reversal SZI triggering is prone to occur under the ideal combination of thermo-mechanical conditions, expressed by older (stronger) DPs and relatively younger (weaker) OPs, that specifically favour this OP-DP coupling and welding.

4.3. Compliance with natural examples

The objective of the present generic numerical modelling was not to study any specific natural case, but rather to gain new insight on the main underlying dynamics governing the occurrence of polarity-reversal SZI for the assumed modelling conditions. This SZI mode has been previously proposed to explain the evolution of different natural tectonic settings (e.g., Kerr et al., 2005; Konstantinovskaia, 2001). In some of these cases, trench-obstruction is thought to have been caused by plateaus of different geological origin, e.g. oceanic ridges or seamounts, submarine volcanic structures and continental fragments (Tetreault and Buiter, 2012), or even by a continental margin attached to the downgoing plate during intra-oceanic subduction (Konstantinovskaia, 2001). In the emblematic example of the Solomon-Vanuatu subduction system polarity-reversal SZI is thought to have occurred during the late Miocene (Fig. 7A), triggered by the arrival of the Ontong-Java Plateau at the North Solomon-Vitiaz subduction zone (Mann and Taira, 2004). In this tectonic setting, the age inferred for the (overriding) Australian oceanic plate lies between 49 and 25 Ma, based on plate tectonic reconstructions (Hall, 2002) and recent regional studies (Mortimer et al., 2014). The age of the polarity-reversal SZI in this subduction system has been proposed to fall between 15 and 5 Ma (Hall, 2002; Schellart et al., 2006). This renders a maximum age interval for the Australian OP at the time of the Ontong-Java plateau docking approximately between 44 and 34 Ma, and a minimum, between 20 and 10 Ma. On the other hand, based on the ~ 150 to 120 Ma age interval deduced for the downgoing Pacific plate (Nikolaeva and Gerya, 2009), its maximum age at docking is calculated between 145 and 135 Ma, whereas its corresponding minimum age would fall between 115 and 105 Ma. Despite some degree of uncertainty expressed by these age intervals, the available evidence conforms well with the general OP-DP plate age combinations that rendered polarity-reversal SZI in our models (i.e., older and stronger DPs paired with younger and weaker OPs). SZI7 experiment illustrates the polarity-reversal possibility for the Solomon-Vanuatu case under the contrasting thermo-mechanical conditions resulting from such plate age combinations (Fig. 7B). In this experiment polarity-reversal SZI is achieved for a relatively younger OP (~ 41 Myr, Fig. 7-B1) fitting the maximum age interval (44 to 34 Ma) for the Australian OP in the natural example. Likewise, a much older DP of ~ 111 Myr in this same experiment also agrees with the minimum age interval (115 to 105 Ma) estimated for the Pacific DP in the natural case (see yellow rectangle in Fig. 4A representing the range of the OP-DP age intervals for the Solomon-Vanuatu example).

4.4. Constraints of present modelling approach

Our models provide new insight on the process of polarity-reversal SZI resulting from the perturbation of the internal driving-force balance on a pre-existent subduction zone. Our restrict premise is thus to consider the internal dynamics of the system (and its thermo-mechanical configuration arising from the contrasting age of the plates involved) as the main governing cause for polarity-reversal triggering. Given this assumption, the adopted 2D modelling simplification of subduction zones could be problematic, since these natural objects are three-dimensional and governed by a dynamics that critically comprises an (inherently 3D) toroidal component of mantle flow (Schellart, 2004; Schellart et al., 2007). Periodic boundary conditions were prescribed to the lateral vertical

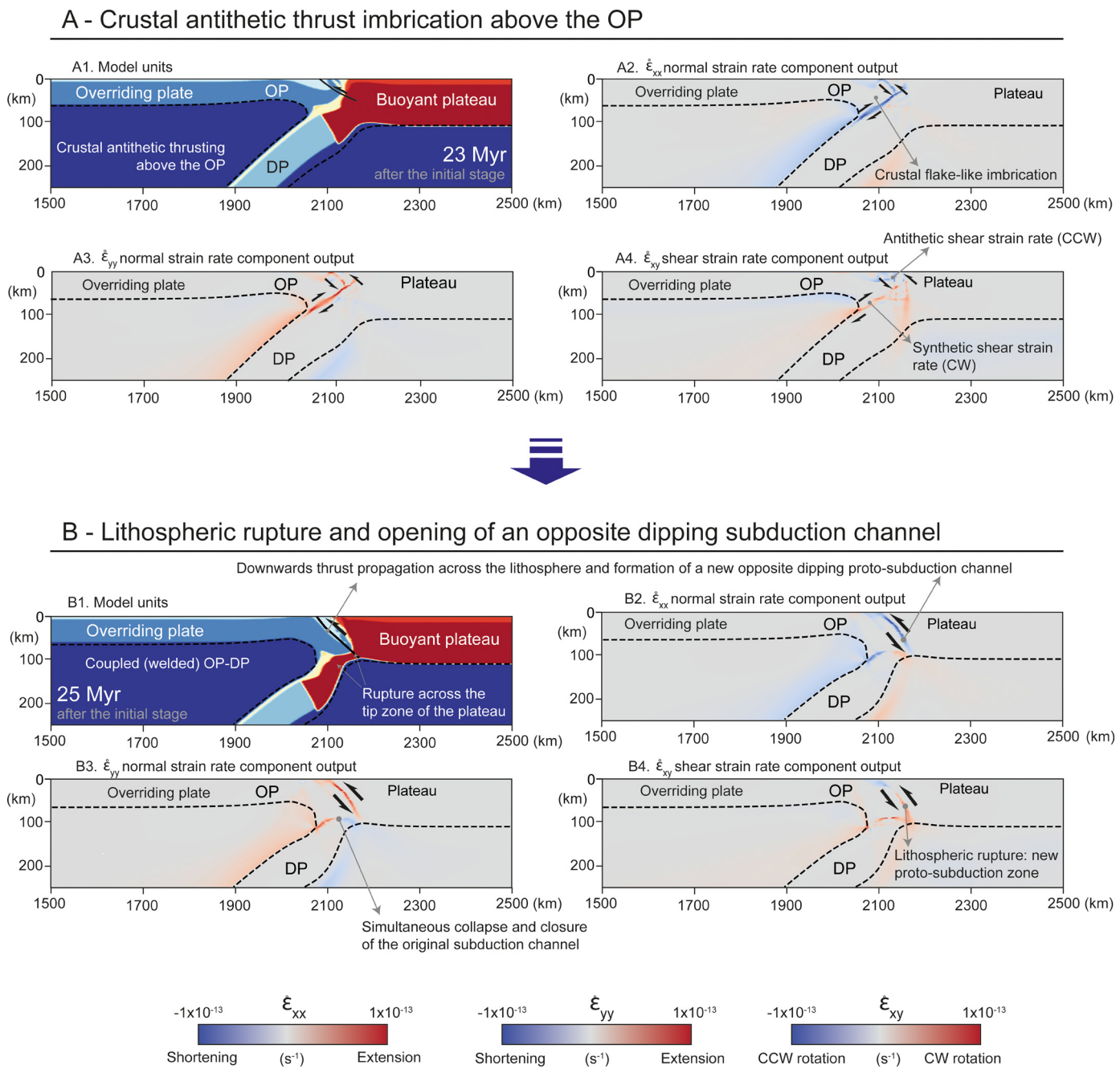

Fig. 5. Model results: polarity-reversal subduction zone initiation (experiment SZI2). Strain rate output illustrating the development of a new opposite dipping subduction channel. **A: Initial antithetic thrust above the overriding plate** yielding crustal flake imbrication (OP); **B: Thrust propagation across the lithosphere** (through the tip of the weaker buoyant plateau) to form a new proto-subduction channel. Simultaneous OP-DP coupling (welding) and closure of the old subduction channel. OP - Overriding plate: DP – Downgoing plate; CW - Clockwise; CCW – Counter-clockwise; Normal ($\dot{\varepsilon}_{xx}$, $\dot{\varepsilon}_{yy}$) and shear ($\dot{\varepsilon}_{xy} = \dot{\varepsilon}_{yx}$) strain rate components of the strain-rate tensor.

walls of our models to avoid mantle flow stagnation beneath the DP slab during roll-back subduction (see section 2.3 above). However, other dynamic effects of mantle toroidal flow on overall plate kinematics and deformation were not accounted for in the present models, which could result in a significant underestimation of the conditions favouring polarity-reversal SZI.

The absence of elasticity in our simulations, while widely adopted in many other modelling studies (Capitanio and Morra, 2012; Gerya and Meilick, 2011; Schellart, 2017; Stegman et al., 2010), is also potentially relevant for our results since it is arguably expected to influence the dynamics of plate bending in subduction systems (e.g., Capitanio and Morra, 2012; Farrington et al., 2014; Thielmann and Kaus, 2012). Also important is the uncertainty pertaining to upper mantle rheology (e.g., Jain and Korenaga, 2020; King, 2016, and references therein) that allows for a somewhat aprioristic choice of parameters, relatively to which the obtained results are expected to be sensitive. This means that a slightly different choice of mantle rheology parameters (in Equation (9) above) corresponding, for instance, to an increase in mantle stiffness, could potentially increase the viscous resistance to slab-pull, thus modifying the underlying governing dynamics of the system and implying considerably different results.

Another model limitation with potential important dynamic consequences for subduction systems, and thus, capable of modifying the polarity-reversal stability field of Fig. 2, is the assumed absence of a mature volcanic arc in the OP above the subduct-

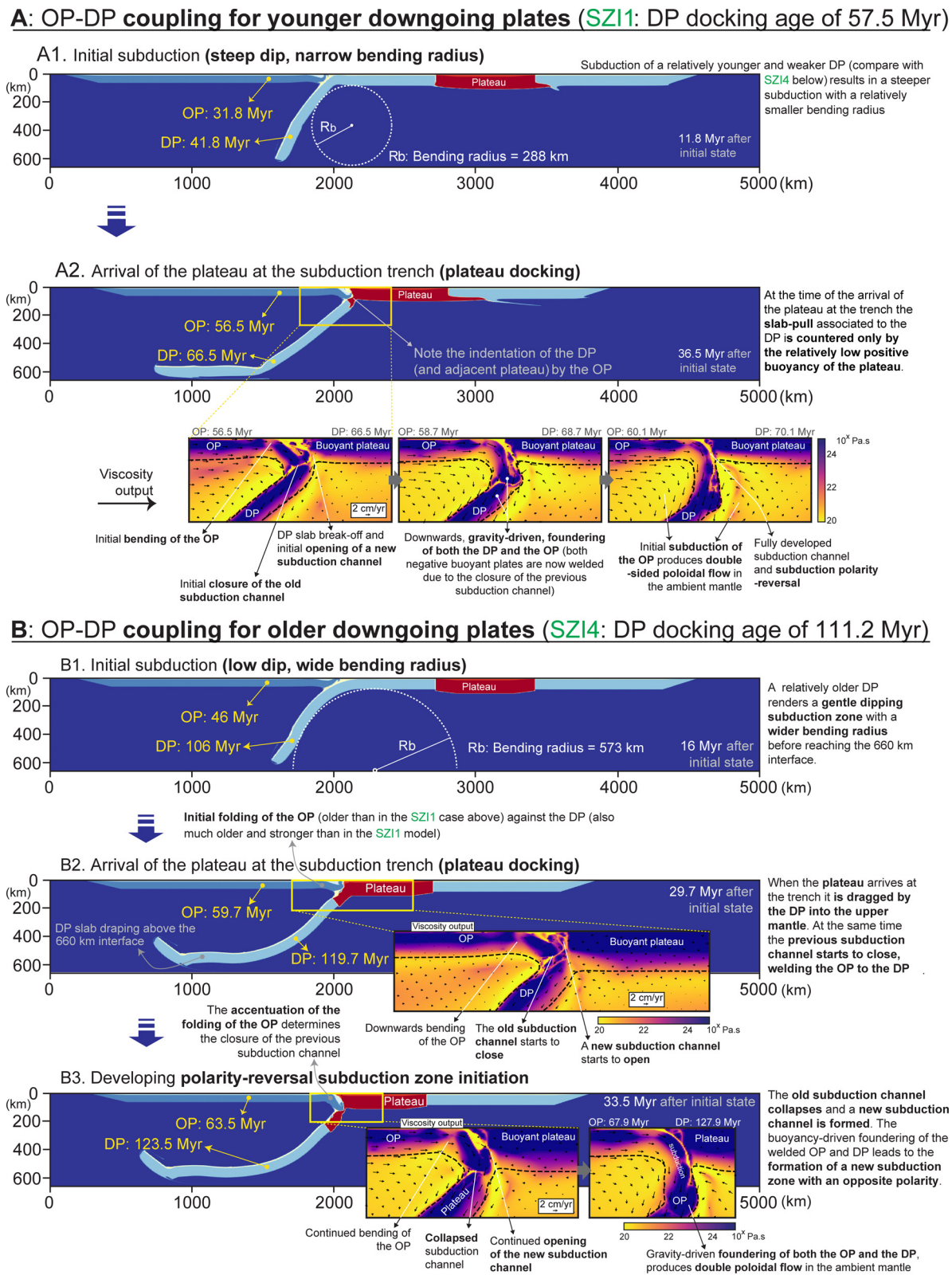

Fig. 6. Prevailing mechanisms of overriding - downgoing plate coupling during polarity-reversal subduction zone initiation. **A**: For relatively young (weak and deformable) downgoing plates (SZI1 model results); **B**: For relatively older (stronger and thicker) downgoing plates (SZI4 model results). OP - Overriding plate: DP – Downgoing plate.

ing slab. Whilst this is a widely assumed standard simplification in many subduction zone models (e.g., Gerya et al., 2008; Gurnis et al., 2004; Lu et al., 2015), natural volcanic arcs could exert a stabilizing effect on the OP, contributing to prevent the occurrence of double-sided subduction in nature (thus increasing the relative frequency of polarity-reversal outcomes).

The sensitiveness of polarity-reversal SZI to the resolution adopted for the numerical modelling experiments is also of critical importance. Robustness of results was only achieved for medium

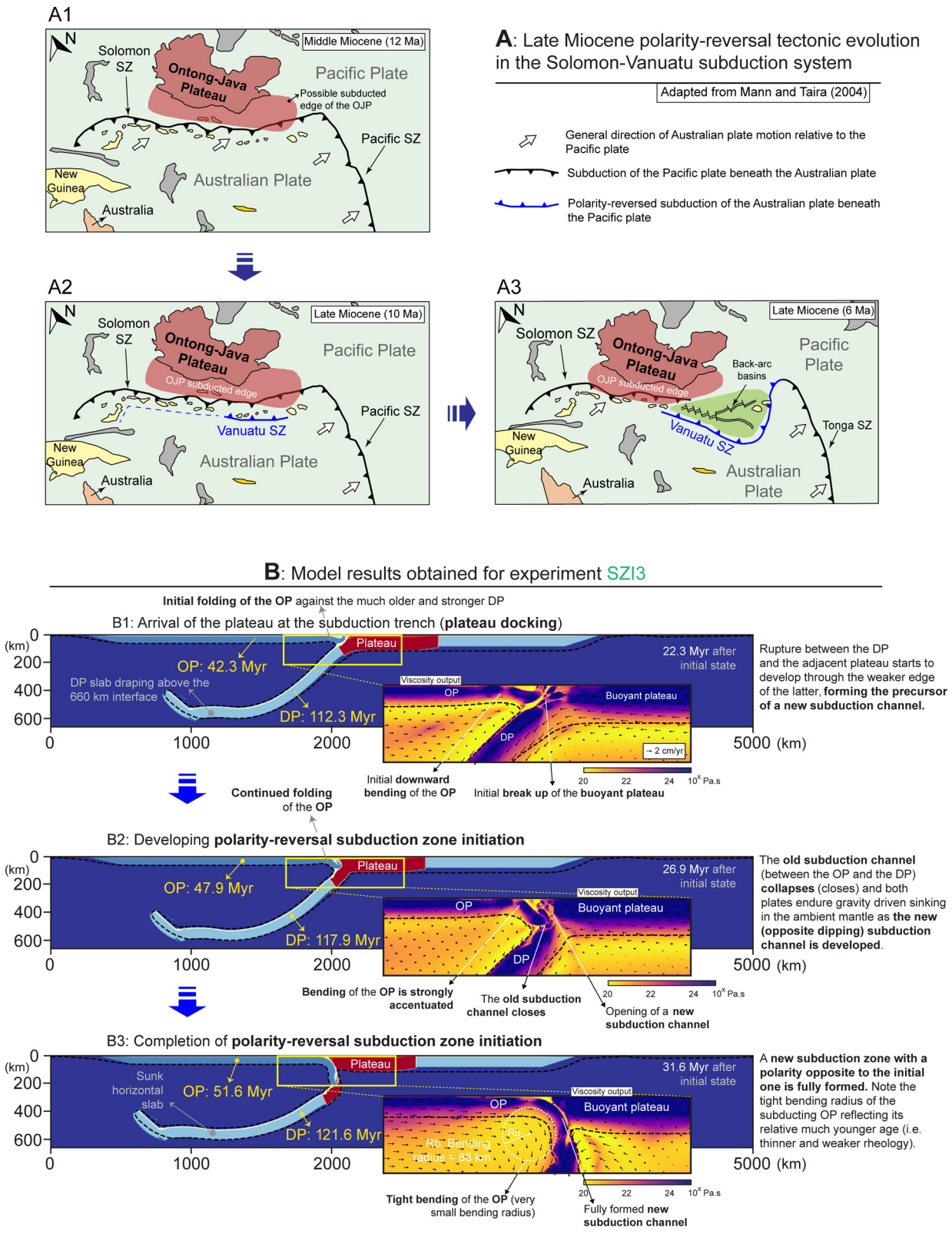

Fig. 7. Example of a natural case in which an oceanic plateau arrives at an active subduction zone and, due to the favourable interplay between resisting and driving forces, led to the development of a new subduction zone by polarity-reversal. **A**: Map depiction of **middle-late Miocene tectonic evolution of the Solomon-Vanuatu subduction systems**, in which the blocking of the North Solomon-Vitiaz subduction trench by the Ontong-Java plateau is interpreted to have triggered polarity-reversal subduction zone initiation, forming the opposite dipping Vanuatu subducting zone (adapted from Mann and Taira, 2004). The initial south dipping North Solomon-Vitiaz subduction zone comprised a much older (stronger and thicker) downgoing Pacific plate (~ 115 to 105 Ma) and a relatively much younger (weaker and thinner) overriding Australian plate (~ 44 to 34 Ma). **A1**: In middle Miocene (12 Ma) the Ontong-Java plateau was already blocking the southwards dipping North Solomon-Vitiaz subduction zone, triggering the polarity-reversal SZI; **A2-A3**: In late Miocene (from ~ 10 to 6 Ma) the new opposite dipping Vanuatu subduction zone is further developed. **B: Model step evolution obtained for SZI3 (polarity-reversal) experiment**, in which the OP, DP docking ages fit the ones of the natural example in A. The subduction polarity-reversal is dynamically driven by the older and much more negatively buoyant DP (age at docking is ~ 112 Ma), against which the much younger, thinner, and deformable OP (age at docking is ~ 42 Ma) is readily folded. OJP – Ontong-Java Plateau; OP - Overriding plate; DP - Downgoing plate; SZ – Subduction zone; dashed black line – Lithosphere-asthenosphere boundary.

to ultra-high resolution tests (see details in Appendix A - Resolution dependency), but important differences arise from considering the carried out numerical experiments at either low or medium resolutions. Since polarity-reversal SZI is crucially dependent on OP-DP coupling, the resolution at which the subduction channel is considered influences the results in each case. Accordingly, low resolutions imply a less efficient localization of strain and a consequent increase in friction along the subduction channel, which favour both early double-sided subduction and polarity-reversal SZI. Conversely, from medium to ultra-high resolutions, the subduction channel becomes much better defined (resolved) rendering strain localization much more effective and decreasing the relative number of polarity-reversal outcomes.

A more exhaustive discussion of these and other (technical) modelling constraints is provided in Appendix A.

5. Conclusions

Our results show how polarity-reversal SZI might be possible to occur under geodynamic conditions similar to the ones considered in our models. These models illustrate how a new opposite dipping subduction zone can form, due to buoyant plateau obstruction of a pre-existent one, in the absence of any far field (external) forces. The experiments depict how certain overriding-downgoing plate age combinations, representing specific thermo-mechanical (rheological) plate configurations, can disturb the inner dynamic balance between (buoyancy driven) slab-pull forces and viscous resistance as to produce polarity-reversal SZI.

The results show that, for the assumed modelling constraints, the scenarios (i.e., plate rheological configurations) which favour polarity-reversal SZI always combine older (stronger and thicker) DPs and relatively younger (weaker and thinner) OPs. This general plate age combination allows for the development of a new subduction channel (while closing the pre-existent one), and for the efficient buoyancy-driven foundering (subduction) of the former OP in the ambient mantle.

Our experiments also show that rheological coupling, or plate welding, between the DP and the OP is key to achieve polarity-reversal SZI for the modelled conditions. This subduction zone initiation mode is thus greatly controlled by the evolving rheological conditions in the subduction channel. Accordingly, our results show that for polarity-reversal SZI to be triggered at the time of plateau docking, a simultaneous decrease in strain localization and increase in friction must occur along the subduction channel, as to eventually cause this channel to collapse and the plates to be welded.

By illustrating the feasibility of polarity-reversal SZI for the restricted conditions implied by our model assumptions, our results suggest that this SZI model might play a more important role than previously anticipated in the cyclic renewal of ocean floors, corresponding to an important process of subduction zone initiation in nature.

CRediT authorship contribution statement

J. Almeida: Conceptualization, Formal analysis, Investigation, Writing – original draft, Writing – review & editing. **N. Riel:** Conceptualization, Investigation, Supervision, Writing – review & editing. **F.M. Rosas:** Investigation, Supervision, Writing – original draft, Writing – review & editing. **J.C. Duarte:** Investigation, Writing – review & editing. **W.P. Schellart:** Investigation, Writing – review & editing.

Declaration of competing interest

The authors declare that they have no known competing financial interests or personal relationships that could have appeared to influence the work reported in this paper.

Acknowledgements

J. Almeida acknowledges funding by FCT PhD grant no. PD/BD/135067/2017 - Earthsystems-IDL. J. Almeida, F.M. Rosas and J.C. Duarte acknowledge financial support by FCT through project UIDB/50019/2020 - IDL. W.P. Schellart has been funded by a Vici Fellowship (016.VICI.170.110) from the Dutch National Science Foundation (NWO). The authors thank Michael Gurnis, Wim Spakman, Fabio Crameri and an anonymous reviewer for their insightful and constructive feedback, which significantly contributed to improve the manuscript.

Appendix A. Model limitations

Modelling techniques intrinsically assume some degree of simplification relatively to the natural process they target (see Zelst et al., 2021 for a discussion). These necessary simplifications imply the sacrifice of details which should not be relevant for the evaluation of the core problems under investigation, and that should be made clear for all. We thus provide the following list of the main model limitations assumed in the present numerical study.

a) 2D modelling approach

Subduction is an intrinsically 3D process in nature since the DP slab width is of key importance for the overall subduction dynamics (Dvorkin et al., 1993; Schellart, 2004; Schellart et al., 2007). A relatively narrow slab allows for mantle material to escape from beneath the DP around its lateral edges, favouring (rollback) slab retreat and significant toroidal flow in the ambient mantle, whereas wide slabs promote mantle flow stagnation under the same subducting DP. Mantle toroidal flow is also responsible for nucleating extension within the OP at a distance of $\sim$ 250 to 400 km from the subduction trench (Duarte et al., 2013b).

The 3D mantle toroidal flow was not accounted for in our 2D models. However, to allow for DP slab-retreat in 2D we adopted periodic boundary conditions for the limiting vertical walls in our models (see Fig. 1A) making it possible for mantle material to escape from beneath the DP by exiting through these boundaries. This avoided the formation of an artificial upper mantle stagnation zone beneath the subducting slab (Schellart et al., 2007), which would adulterate the dynamics of the sinking DP. Additionally, the overall dimensions of the model were always prescribed to be larger than the generated mantle flow cells.

The toroidal flow-related extension within the OP is predicted to nucleate at a distance from the trench ($\sim$ 200 km) similar to the one at which the main hinge of the OP downwards bending is located in our polarity-reversal SZI experiments. This suggests that the influence of the 3D mantle toroidal flow in the overlying OP would tend to facilitate polarity-reversal SZI, and thus, that our 2D results might correspond to an underestimation of its occurrence in nature.

b) Absence of a volcanic arc

As in many previous studies (Gerya et al., 2008; Gurnis et al., 2004; Lu et al., 2015), the absence of a volcanic arc has been adopted as a simplification in our numerical models. To our knowledge, no previous numerical modelling approach has systematically investigated the role of volcanic arcs in the overall dynamic control of subduction zones. However, the ubiquitous presence of arcs in

all active intra-oceanic subduction zones suggests they might contribute, not only to thermo-mechanically stabilize the tip of the OP by adding to its positive buoyancy, but also to act as an effective mechanism for reducing the strength of this plate (Gerya and Meilick, 2011). As such, the presence of an arc in the OP could widen the domain of conditions under which polarity-reversal SZI could occur, contributing to a reduction in the number of unstable double-sided subduction results (see Fig. 2). On the other hand, the presence of a positive buoyant arc could also impede polarity-reversal SZI by holding the leading edge of the overriding plate at the surface. However, in such a situation, it is also possible that the crustal flake-like imbrication observed in our models (Fig. 5A) could be responsible for scraping off the buoyant volcanic arc atop one of the main antithetic thrusts propagating further into the OP (undercutting the buoyant arc crust). This would lead to accretion of the arc to the DP, separating it from the negatively buoyant OP, and thereby allowing polarity-reversal SZI to happen.

c) Absence of elastic behaviour

In our numerical study the elasticity of lithospheric plates was not accounted for. As in several other previous contributions (e.g., Capitanio and Morra, 2012; Gerya and Meilick, 2011; Schellart, 2017; Stegman et al., 2010), the rheological behaviour of the lithosphere and upper mantle was here prescribed to follow strictly visco-plastic laws. The role of elastic behaviour in facilitating or hindering the bending of the DP slab in subduction systems has been discussed by Farrington et al. (2014), who considered that subduction slab geometry, subduction angle, and the amount of slab draping (above the 660 km basal discontinuity) were mostly unaffected by elasticity. Instead, the subduction regime is thought as mostly dependent on the relative viscosity/density contrasts between the lithosphere and upper mantle (e.g., Capitanio and Morra, 2012). Additionally, the role of elasticity in the formation of lithospheric-scale weaknesses (i.e., new subduction channels) was explored in Thielmann and Kaus (2012). They showed that the inclusion of elastic behaviour, as opposed to pure visco-plastic laws, delayed the formation of lithospheric-scale weak zones, which however, once formed, would be more efficiently localized.

We acknowledge that the potential effects of direct or induced elasticity (i.e., plate stiffness) in the bending of the OP during polarity-reversal SZI remain largely unknown. We anticipate that these effects are probably complex and non-linear, as illustrated by the fact that a less pronounced plate bending may often translate into a lower energy dissipation involved in the subduction process (Irvine and Schellart, 2012). Also, initial OP bending, while potentially affected by the elastic properties of the oceanic crust, might lead to elastic stress weakening at the bending hinge (Farrington et al., 2014), causing a decrease in the plate bending radius. Finally, elastic behaviour is likely to help localizing the new subduction channel (Thielmann and Kaus, 2012) during plateau collision. As such, we acknowledge that further future modelling is required to precisely clarify the role of elasticity in polarity reversal SZI processes.

d) Simplified oceanic plateau

Our oceanic plateau was simplified as corresponding always to an overthickened segment of oceanic lithosphere, and never to a continental block. This implies that our oceanic plateau has a thermo-rheological profile identical to the one of an oceanic plate, i.e., with a simple (single) transition between a brittle lithosphere and a ductile upper (asthenospheric) mantle. By contrast, continental lithosphere typically shows a more complex rheological structure, comprising a brittle-ductile upper to lower crust transition, and a similar mantle lithosphere to asthenosphere transition (e.g. Kohlstedt et al., 1995). In the latter case, the existence of a ductile intermediate layer (between the brittle upper crust and the upper lithospheric mantle) allows for the formation of a decollement between the continental crust and the mantle (e.g., Koptev et al., 2019). As such, during plateau docking, the crustal portion of a continental plateau could be antithetically thrusted and accreted on top of the overriding plate, while its corresponding mantle portion would continue to subduct. This would thus favour the formation of a wedge-like structure (flake imbrication) like the one observed in our models (see Fig. 5A), which according to our results precludes polarity-reversal SZI if OP-DP plate welding is also achieved.

e) Upper mantle rheology uncertainty

At present, the rheology of the upper mantle is not entirely understood, and the corresponding constraints assumed in most numerical modelling approaches are essentially based on experimental mechanical studies of peridotites and olivines (e.g., Escartín et al., 2001; Hui et al., 2014). This uncertainty is relevant for our model results, since slight variations within the range of admissible parameters for the rheology of mantle could lead to markedly different outcomes. A stronger upper mantle rheology could contribute to a more efficient localization of the deformation making it more difficult for plate welding to occur. At the same time, it would also imply a higher viscous resistance to the slab-pull forces, significantly modifying the overall dynamics of the subduction system. Therefore, a slightly different upper mantle rheology could very well change the polarity-reversal stability field suggested by the present modelling results.

f) Resolution dependency

Model resolution can have an impact on the obtained numerical results, since the dynamics governing the target (tectonic system) under scrutiny is not necessarily scale independent. This means that for an overall similar geometry, e.g., a same subduction channel, the detailed rheological configuration and associated stress distribution across the channel might be sensitive to the resolved thickness of the corresponding shear zone in different cases. Different resolutions might thus imply different dynamic conditions, and therefore, different geometrical/kinematical model results (Arcay, 2017; Kaus, 2009; Sandiford and Moresi, 2019; Schellart and Moresi, 2013).

To gain some insight on the general resolution sensitivity of our models, we ran an initial set of 63 experiments (Supplementary Figure 1) using two main different resolutions: 768×192 (medium resolution - MR) and 1536×384 (high resolution - HR). The results showed that the unstable double-sided subduction is much less frequent at higher resolutions (changing from 37% at MR to 8% at HR, see Supplementary Figure 1). HR results also showed that polarity-reversal SZI does not occur for conditions characterized by younger DP ages, shifting the stability field for this outcome towards conditions preferably characterized by older DPs and relatively younger OPs. This suggests that the OP-DP coupling (i.e., plate welding) in polarity-reversal outcomes involving younger plates corresponds to an artificial effect, determined by the less efficient strain localization implied by the low resolution. Accordingly, a poorer definition of rheology (and a less detailed stress distribution configuration) in the subduction channel artificially favours the coupling between both plates and the consequent frequency of both polarity-reversal SZI and double-sided subduction. Conversely, in HR trials the subduction channel would be sufficiently resolved (sharpened and defined) to allow for an efficient strain localization, and to favour a more “realistic”, dynamically driven, polarity-reversal outcome.

Further resolution tests of polarity-reversal SZI were carried out to evaluate the robustness of the polarity-reversal outcome under the thermo-mechanical conditions implied by a combination of

older DPs and younger OPs. This was done by running models at four different resolutions comprising an OP of 20 Myrs, paired with a DP of 90 Myrs (black square in Supplementary Figure 1). Thus, besides the MR and HR trials, two other resolutions were additionally considered in this case: a lower most one of 384×96 (low resolution - LR), and a higher one of 2304×576 (ultra-high - UHR). The obtained test results show general coherent polarity-reversal SZI for almost all the tested resolutions, except in the LR case, in which efficient strain localization is not attained along the subduction channel, triggering early double-sided subduction instead (Supplementary Video 8). In the UHR case the accomplishment of polarity-reversal SZI takes more than double the time observed for the other models (MR and HR cases, Supplementary Video 8). This is probably due to a much widespread dissipation of the same initial energy, implied by the much higher resolution in this case, which ultimately also expresses a change in the overall dynamics of the model.

It is clear from these tests that changing the resolution significantly changes the dynamics of the modelled subduction zone. Although in the present case some degree of resolution robustness was achieved for relevant OP-DP initial age conditions, resolution dependence potentially constitutes an important limitation in the numerical modelling of subduction polarity reversal, introducing additional non-linearity to models and changing the underlying governing dynamics for different considered resolutions.

g) Lack of a free surface

The use of free-slip top boundary conditions in subduction models was previously reported as favouring double-sided subduction outcomes (e.g., Crameri et al., 2012; Schmeling et al., 2008). While most of our results obtained for free slip top BCs show the development of single-sided asymmetric subduction zones, a small percentage does lead to the formation of double-sided subduction zones (five out of 77 models, ca. 6%, Fig. 2).

Since double-sided subduction zones have never been found in nature (Gerya et al., 2008), we have interpreted their occurrence in the present study as mostly corresponding to model artefacts. Our results show that these unnatural subduction outcomes are scarce, occurring only for the weakest/youngest overriding plates (10 My, see Fig. 2), which are unable to resist the stresses imposed by the sinking and trench-retreat of the subducting slab from early stages of the experiments. As reported by the authors cited above, this propensity to bend downwards and subduct would be further facilitated by the here adopted top free-slip BCs (instead of free surface).

Moreover, the combination of young overriding plates and old downgoing ones also closely corresponds to the unravelled stability field for the occurrence of polarity-reversal SZI (Fig. 2). As such, the implementation of top free surface BCs in our models (instead of the adopted free slip) could result in the reduction, or even the elimination, of the double-sided subduction outcome yielding, for the same conditions, polarity reversal SZI instead. Accordingly, free surface BCs would make it more difficult for the young overriding plates to be bent downwards and to subduct, lessening the frequency of the double-sided subduction outcome. This concurs with the possible underestimation of polarity reversal results in our models relatively to nature, which could also result from other causes (as discussed in paragraphs a and b above).

Appendix B. Supplementary material

Supplementary material related to this article can be found online at https://doi.org/10.1016/j.epsl.2021.117195.

References

Arcay, D., Lallemand, S., Abecassis, S., Garel, F., 2019. Can subduction initiation at a transform fault be spontaneous? Solid Earth Discuss. 1 (34). https://doi.org/10.5194/se-2019-63.

Auzemery, A., Willingshofer, E., Yamato, P., Duretz, T., Sokoutis, D., 2020. Strain localization mechanisms for subduction initiation at passive margins. Glob. Planet. Change 195, 103323. https://doi.org/10.1016/j.gloplacha.2020.103323.

Buchs, D.M., Arculus, R.J., Baumgartner, P.O., Baumgartner-Mora, C., Ulianov, A., 2010. Late Cretaceous arc development on the SW margin of the Caribbean Plate: insights from the Golfito, Costa Rica, and Azuero, Panama, complexes. Geochem. Geophys. Geosyst. 11. https://doi.org/10.1029/2009GC002901.

Capitanio, F.A., Morra, G., 2012. The bending mechanics in a dynamic subduction system: constraints from numerical modelling and global compilation analysis. Tectonophysics 522–523, 224–234. https://doi.org/10.1016/j.tecto.2011.12.003.

Cloetingh, S., Wortel, R., Vlaar, N.J., 1989. On the initiation of subduction zones. Pure Appl. Geophys. 129, 7–25. https://doi.org/10.1007/BF00874622.

Cloetingh, S.A.P.L., Wortel, M.J.R., Vlaar, N.J., 1982. Evolution of passive continental margins and initiation of subduction zones. Nature 297, 139–142. https://doi.org/10.1038/297139a0.

Crameri, F., Magni, V., Domeier, M., Shephard, G.E., Chotalia, K., Cooper, G., Eakin, C.M., Grima, A.G., Gürer, D., Király, Á., Mulyukova, E., Peters, K., Robert, B., Thielmann, M., 2020. A transdisciplinary and community-driven database to unravel subduction zone initiation. Nat. Commun. 11, 1–14. https://doi.org/10.1038/s41467-020-17522-9.

Crameri, F., Tackley, P.J., 2015. Parameters controlling dynamically self-consistent plate tectonics and single-sided subduction in global models of mantle convection. J. Geophys. Res., Solid Earth 120, 3680–3706. https://doi.org/10.1002/2014JB011664.

Crameri, F., Tackley, P.J., Foley, B.J., Becker, T.W., 2014. Spontaneous development of arcuate single-sided subduction in global 3-D mantle convection models with a free surface. J. Geophys. Res., Solid Earth 119, 5921–5942. https://doi.org/10.1002/2014JB010939.

Davies, G.F., 1992. On the emergence of plate tectonics. Geology 20, 963. https://doi.org/10.1130/0091-7613(1992)020<0963:OTEOPT>2.3.CO;2.

Drucker, D.C., Prager, W., 1952. Soil mechanics and plastic analysis or limit design. Q. Appl. Math. 10, 157–165. https://doi.org/10.1090/qam/48291.

Duarte, J.C., Rosas, F.M., Terrinha, P., Schellart, W.P., Boutelier, D., Gutscher, M.-A., Ribeiro, A., 2013a. Are subduction zones invading the Atlantic? Evidence from the southwest Iberia margin. Geology 41. https://doi.org/10.1130/G34100.1.

Duarte, J.C., Schellart, W.P., Cruden, A.R., 2013b. Three-dimensional dynamic laboratory models of subduction with an overriding plate and variable interplate rheology. Geophys. J. Int. 195, 47–66. https://doi.org/10.1093/gji/ggt257.

Farrington, R.J., Moresi, L.-N., Capitanio, F.A., 2014. The role of viscoelasticity in subducting plates. Geochem. Geophys. Geosyst. 15, 4291–4304. https://doi.org/10.1002/2014GC005507.

Gerya, T.V., Connolly, J.A.D., Yuen, D.A., 2008. Why is terrestrial subduction one-sided? Geology 36, 43. https://doi.org/10.1130/G24060A.1.

Gerya, T.V., Meilick, F.I., 2011. Geodynamic regimes of subduction under an active margin: effects of rheological weakening by fluids and melts. J. Metamorph. Geol. 29, 7–31. https://doi.org/10.1111/j.1525-1314.2010.00904.x.

Gurnis, M., Hall, C., Lavier, L., 2004. Evolving force balance during incipient subduction. Geochem. Geophys. Geosyst. 5. https://doi.org/10.1029/2003GC000681.

Hall, R., 2019. The subduction initiation stage of the Wilson cycle. Geol. Soc. (Lond.) Spec. Publ. 470, 415–437. https://doi.org/10.1144/SP470.3.

Hall, R., 2002. Cenozoic geological and plate tectonic evolution of SE Asia and the SW Pacific: computer-based reconstructions, model and animations. J. Asian Earth Sci. 20, 353–431. https://doi.org/10.1016/S1367-9120(01)00069-4.

Hirauchi, K., Fukushima, K., Kido, M., Muto, J., Okamoto, A., 2016. Reaction-induced rheological weakening enables oceanic plate subduction. Nat. Commun. 7, 12550. https://doi.org/10.1038/ncomms12550.

Hui, Y., Xueliang, J., Na, L., 2014. Experimental study on mechanical property of peridotite under water-rock interaction test procedure. Electron. J. Geotech. Eng. 19E, 1179–1188.

Irvine, D.N., Schellart, W.P., 2012. Effect of plate thickness on bending radius and energy dissipation at the subduction zone hinge. J. Geophys. Res., Solid Earth 117, 1–14. https://doi.org/10.1029/2011JB009113.

Jain, C., Korenaga, J., 2020. Synergy of experimental rock mechanics, seismology, and geodynamics reveals still elusive upper mantle rheology. J. Geophys. Res., Solid Earth 125, e2020JB019896. https://doi.org/10.1029/2020JB019896.

Kerr, A.C., White, R.V., Thompson, P.M.E., Tarney, J., Saunders, A.D., 2005. No oceanic plateau - no Caribbean plate? The seminal role of an oceanic plateau in Caribbean plate evolution. In: AAPG Mem., pp. 23–26.

King, S.D., 2016. Reconciling laboratory and observational models of mantle rheology in geodynamic modelling. J. Geodyn. 100, 33–50. https://doi.org/10.1016/j.jog.2016.03.005.

Konstantinovskaia, E., 2001. Arc–continent collision and subduction reversal in the Cenozoic evolution of the Northwest Pacific: an example from Kamchatka (NE Russia). Tectonophysics 333, 75–94. https://doi.org/10.1016/S0040-1951(00)00268-7.

Lu, G., Kaus, B.J.P., Zhao, L., Zheng, T., 2015. Self-consistent subduction initiation induced by mantle flow. Terra Nova 27, 130–138. https://doi.org/10.1111/ter.12140.

Mann, P., Taira, A., 2004. Global tectonic significance of the Solomon Islands and Ontong Java Plateau convergent zone. Tectonophysics 389, 137–190. https://doi.org/10.1016/j.tecto.2003.10.024.

Moresi, L., Quenette, S., Lemiale, V., Mériaux, C., Appelbe, B., Mühlhaus, H.B., 2007. Computational approaches to studying non-linear dynamics of the crust and mantle. Phys. Earth Planet. Inter. 163, 69–82. https://doi.org/10.1016/j.pepi.2007.06.009.

Mortimer, N., Gans, P.B., Palin, J.M., Herzer, R.H., Pelletier, B., Monzier, M., 2014. Eocene and Oligocene basins and ridges of the Coral Sea-New Caledonia region: tectonic link between Melanesia, Fiji, and Zealandia. Tectonics 33, 1386–1407. https://doi.org/10.1002/2014TC003598.

Mueller, S., Phillips, R.J., 1991. On the initiation of subduction. J. Geophys. Res. 96, 651. https://doi.org/10.1029/90JB02237.

Nikolaeva, K., Gerya, T.V., Marques, F.O., 2011. Numerical analysis of subduction initiation risk along the Atlantic American passive margins. Geology 39, 463–466. https://doi.org/10.1130/G31972.1.

Nikolaeva, K., Gerya, T.V., Marques, F.O., 2010. Subduction initiation at passive margins: numerical modeling. J. Geophys. Res., Solid Earth 115, 1–19. https://doi.org/10.1029/2009JB006549.

Nikolaeva, K.M., Gerya, T.V., 2009. Numerical modeling of intraoceanic arc growth. Moscow Univ. Geol. Bull. 64, 230–243. https://doi.org/10.3103/S0145875209040048.

Ranalli, G., 1997. Rheology and deep tectonics. Ann. Geofis. https://doi.org/10.4401/ag-3893.

Schellart, W.P., 2017. Andean mountain building and magmatic arc migration driven by subduction-induced whole mantle flow. Nat. Commun. 8, 1–13. https://doi.org/10.1038/s41467-017-01847-z.

Schellart, W.P., 2004. Kinematics of subduction and subduction-induced flow in the upper mantle. J. Geophys. Res. B Solid Earth 109, 1–19. https://doi.org/10.1029/2004JB002970.

Schellart, W.P., Freeman, J., Stegman, D.R., Moresi, L., May, D., 2007. Evolution and diversity of subduction zones controlled by slab width. Nature 446, 308–311. https://doi.org/10.1038/nature05615.

Schellart, W.P., Lister, G.S., Toy, V.G., 2006. A Late Cretaceous and Cenozoic reconstruction of the Southwest Pacific region: tectonics controlled by subduction and slab rollback processes. Earth-Sci. Rev. 76, 191–233. https://doi.org/10.1016/J.EARSCIREV.2006.01.002.

Stegman, D.R., Farrington, R., Capitanio, F.A., 2010. A regime diagram for subduction styles from 3-D numerical models of free subduction. Tectonophysics 483, 29–45. https://doi.org/10.1016/J.TECTO.2009.08.041.

Stern, R.J., 2004. Subduction initiation: spontaneous and induced. Earth Planet. Sci. Lett. 226, 275–292. https://doi.org/10.1016/j.epsl.2004.08.007.

Stern, R.J., Gerya, T., 2018. Subduction initiation in nature and models: a review. Tectonophysics. https://doi.org/10.1016/j.tecto.2017.10.014.

Tetreault, J.L., Buiter, S.J.H., 2012. Geodynamic models of terrane accretion: testing the fate of island arcs, oceanic plateaus, and continental fragments in subduction zones. J. Geophys. Res., Solid Earth 117, 1–23. https://doi.org/10.1029/2012JB009316.

Thielmann, M., Kaus, B.J.P., 2012. Shear heating induced lithospheric-scale localization: does it result in subduction? Earth Planet. Sci. Lett. 359–360, 1–13. https://doi.org/10.1016/j.epsl.2012.10.002.

Uyeda, S., Ben-Avraham, Z., 1972. Origin and development of the Philippine Sea. Nature 238, 37. https://doi.org/10.1038/physci240176a0.

Wright, J.E., Wyld, S.J., 2011. Late Cretaceous subduction initiation on the eastern margin of the Caribbean-Colombian Oceanic Plateau: One Great Arc of the Caribbean (?). Geosphere 7, 468–493. https://doi.org/10.1130/GES00577.1.

Zhang, S., Leng, W., 2021. Subduction polarity reversal: induced or spontaneous? Geophys. Res. Lett. 48 (11), 1–11. https://doi.org/10.1029/2021GL093201.

Zhong, X., Li, Z., 2019. Forced subduction initiation at passive continental margins: velocity-driven versus stress-driven. Geophys. Res. Lett. 46, 11054–11064. https://doi.org/10.1029/2019GL084022.

References (Appendix)

Arcay, D., 2017. Modelling the interplate domain in thermo-mechanical simulations of subduction: critical effects of resolution and rheology, and consequences on wet mantle melting. Phys. Earth Planet. Inter. 269, 112–132. https://doi.org/10.1016/j.pepi.2017.05.008.

Crameri, F., Tackley, P.J., Meilick, I., Gerya, T.V., Kaus, B.J.P., 2012. A free plate surface and weak oceanic crust produce single-sided subduction on Earth. Geophys. Res. Lett. 39, 1–7. https://doi.org/10.1029/2011GL050046.

Dvorkin, J., Nur, A., Mavko, G., Ben-Avraham, Z., 1993. Narrow subducting slabs and the origin of backarc basins. Tectonophysics 227, 63–79. https://doi.org/10.1016/0040-1951(93)90087-Z.

Escartín, J., Hirth, G., Evans, B., 2001. Strength of slightly serpentinized peridotites: implications for the tectonics of oceanic lithosphere. Geology 29, 1023–1026. https://doi.org/10.1130/0091-7613(2001)029<1023:SOSSPI>2.0.CO;2.

Kaus, B.J.P., 2009. Factors that control the angle of shear bands in geodynamic numerical models of brittle deformation. https://doi.org/10.1016/j.tecto.2009.08.042.

Kohlstedt, D.L., Evans, B., Mackwell, S.J., 1995. Strength of the lithosphere: constraints imposed by laboratory experiments. J. Geophys. Res. 100, 17587–17602. https://doi.org/10.1029/95JB01460.

Koptev, A., Ehlers, T.A., Nettesheim, M., Whipp, D.M., 2019. Response of a rheologically stratified lithosphere to subduction of an indenter-shaped plate: insights into localized exhumation at orogen syntaxes. Tectonics 38, 1908–1930. https://doi.org/10.1029/2018TC005455.

Sandiford, D., Moresi, L., 2019. Improving subduction interface implementation in dynamic numerical models. https://doi.org/10.5194/se-2019-11.

Schellart, W.P., Moresi, L., 2013. A new driving mechanism for backarc extension and backarc shortening through slab sinking induced toroidal and poloidal mantle flow: results from dynamic subduction models with an overriding plate. J. Geophys. Res., Solid Earth 118, 3221–3248. https://doi.org/10.1002/jgrb.50173.

Schmeling, H., Babeyko, A.Y., Enns, A., Faccenna, C., Funiciello, F., Gerya, T., Golabek, G.J., Grigull, S., Kaus, B.J.P., Morra, G., Schmalholz, S.M., van Hunen, J., 2008. A benchmark comparison of spontaneous subduction models-towards a free surface. Phys. Earth Planet. Inter. 171, 198–223. https://doi.org/10.1016/j.pepi.2008.06.028.

Van Zelst, I., Crameri, F., Pusok, A.E., Glerum, A., Dannberg, J., 2021. 101 Geodynamic modelling: how to design, carry out, and interpret numerical studies. Solid Earth Discuss. https://doi.org/10.5194/se-2021-14. Preprint.